e-ISSN 2150-5551
CN 31-2103/TB

Nano-Micro Letters

ARTICLE

https://doi.org/10.1007/s40820-024-01528-9

Cite as
Nano-Micro Lett.
(2025) 17:11

Received: 8 June 2024
Accepted: 1 September 2024

Boosting Oxygen Evolution Reaction Performance on NiFe-Based Catalysts Through *d*-Orbital Hybridization

Xing Wang[1], Wei Pi[1], Sheng Hu[1], Haifeng Bao[1] ✉, Na Yao[1] ✉, Wei Luo[2] ✉

HIGHLIGHTS

- The NiFeLa catalyst with 3*d*-5*d* orbital coupling exhibits remarkable oxygen evolution reaction (OER) activity and stability, enabling an anion-exchange membrane water electrolyzers device to achieve a cell voltage of only 1.58 V at 1 A cm^{-2} as well as long-term stability over 600 h.
- The introduction of La disrupts the symmetry of Ni-Fe units and optimize d band center, which affects the *d-p* orbital hybridization between the metal sites on the surface of the catalyst and oxygen-containing intermediates during the OER process.
- The 5*d*-introduced NiFeLa has enhanced adsorption strength of oxygen intermediates, which can reduce the rate-determining step energy barrier and prevent catalyst dissolution.

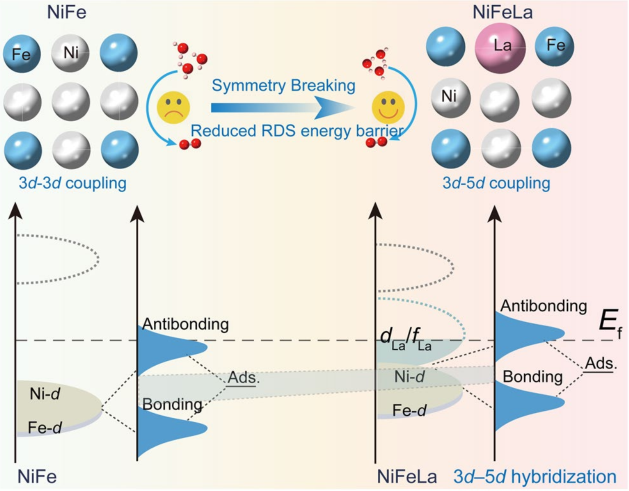

ABSTRACT Anion-exchange membrane water electrolyzers (AEMWEs) for green hydrogen production have received intensive attention due to their feasibility of using earth-abundant NiFe-based catalysts. By introducing a third metal into NiFe-based catalysts to construct asymmetrical M-NiFe units, the *d*-orbital and electronic structures can be adjusted, which is an important strategy to achieve sufficient oxygen evolution reaction (OER) performance in AEMWEs. Herein, the ternary NiFeM (M: La, Mo) catalysts featured with distinct M-NiFe units and varying *d*-orbitals are reported in this work. Experimental and theoretical calculation results reveal that the doping of La leads to optimized hybridization between *d* orbital in NiFeM and 2*p* in oxygen, resulting in enhanced adsorption strength of oxygen intermediates, and reduced rate-determining step energy barrier, which is responsible for the enhanced OER performance. More critically, the obtained NiFeLa catalyst only requires 1.58 V to reach 1 A cm^{-2} in an anion exchange membrane electrolyzer and demonstrates excellent long-term stability of up to 600 h.

KEYWORDS NiFe-based catalysts; *d*-orbital coupling; Oxygen evolution reaction; Anion exchange membrane electrolyzer

---

Xing Wang and Wei Pi contributed equally to the work.
✉ Haifeng Bao, baohaifeng@wtu.edu.cn; Na Yao, yaona@wtu.edu.cn; Wei Luo, wluo@whu.edu.cn
[1] State Key Laboratory of New Textile Materials and Advanced Processing Technology, Key Laboratory of New Textile Materials and Applications of Hubei Province, School of Materials Science and Engineering, Wuhan Textile University, Wuhan 430200, People's Republic of China
[2] College of Chemistry and Molecular Sciences, Wuhan University, Wuhan 430072, People's Republic of China

1 Introduction

Oxygen evolution reaction (OER), a pivotal role in exploiting clean and renewable hydrogen, offers a pathway to reduce the dependence on fossil fuels and achieve carbon neutrality [1–5]. Essentially, the OER process accompanies four proton-coupled electrochemical reactions, typically resulting in sluggish reaction kinetics and poor electrochemical performance [6–8]. In the past decades, substantial scholarly efforts have been dedicated to the refinement of OER electrocatalysts, aimed at optimizing the intricate four-electron transfer reaction pathways, featuring materials such as transition metal oxides, layered structures, and perovskites [9–11]. In recent years, NiFe-based catalysts (e.g., (oxy) hydroxides, alloys, coordination polymers, nitrides, sulfides, and carbides) have attracted widespread attention [12–17]. However, their OER activities still fall short of expectations due to the higher energy barrier associated with the rate-determining step (RDS) [18–20]. Therefore, it is still urgent to discover effective approaches to overcome the sluggish RDS energy barrier, and further improve the OER performance of NiFe-based OER electrocatalysts.

Currently, the electronic modulation strategy provides rational direction in optimizing the intrinsic activity of electrocatalysts by balancing the adsorption of intermediates [12, 21, 22]. For NiFe-based catalysts, the adsorption of oxygen intermediates is primarily correlated with the *d*-band electron structure, which is mainly determined by the *d*-orbital structure [23–25]. Due to the symmetry breaking caused by the doping of different atoms, the *d* orbital structure can be rational regulated [26, 27]. For example, Fu and co-workers achieved high activity and stability of P-Ce SAS@CoO materials by constructing the asymmetric Co–O–Ce unit sites. They found that the enhanced adsorption of oxygen intermediates by optimizing the Co-3*d* orbital electron structure through *d-f* gradient orbital coupling was responsible for the enhanced OER activity [28]. Considering different positions of *5d*/*4d*/*3d*/*3d* energy levels relative to E_f, as well as various orbital coupling effects, it is expected that different elements will construct different asymmetric M-M unit sites, and optimize *d*-orbital structures [29–32]. Despite considerable efforts have been achieved, the catalytic mechanism based on the different *5d*/*4d*/*3d*-introduced orbital and electronic structures for RDS during OER process have rarely been investigated.

In this work, we have successfully manufactured a new class of NiFeM ($M=$ Mo, La) electrocatalysts via electrodeposition method. In particular, 5*d*-La introduced NiFeLa displays an ultralow overpotential of 190 mV at 10 mA cm^{-2} and an ultralong stability of 600 h at 100 mA cm^{-2} in 1 M KOH. Impressively, an anion-exchange membrane water electrolyzer (AEMWE) using NiFeLa as anode catalyst can operate stably for 600 h at 1 A cm^{-2}. Experimental and theoretical calculations show that the introduction of La atoms into NiFe disrupts the symmetry of the Ni–Fe units and constructs 3*d*-5*d* orbital coupled Ni/Fe-M asymmetric geometric structure, leading to optimized *d-p* orbital hybridization between the metal sites on the surface of the catalyst and oxygen-containing intermediates, as well as promoted electron transfer and adsorption of oxygen intermediates.

2 Experimental Section

2.1 Materials

All chemicals were used as received. Ferric chloride hexahydrate ($FeCl_3 \cdot 6H_2O, \geq 99\%$), Nickel chloride hexahydrate ($NiCl_2 \cdot 6H_2O, \geq 97\%$), Sodium chloride ($NaCl, \geq 99.8\%$), Sodium molybdate anhydrous ($Na_2MoO_4, \geq 99\%$), Lanthanum nitrate hexahydrate ($La(NO_3)_3 \cdot 6H_2O, \geq 99\%$) were purchased from Sinopharm Chemical Reagent Co., Ltd. The carbon cloth (WOS 1011) was obtained from CeTech. Milli-Q purification system was used to obtain high-purity water.

2.2 Fabrication of NiFeLa Alloys with Varying Amounts of La

15 mmol of $NiCl_2 \cdot 6H_2O$, 5 mmol of $FeCl_3 \cdot 6H_2O$, 10 mmol of NaCl and a certain amount of $La(NO_3)_3 \cdot 6H_2O$ (0.25, 0.5, 1, and 1.5 mmol) were dissolved in 100 mL ultrapure water. A graphite rod was used as counter electrode, a standard Hg/HgO electrode was used as reference electrode, and carbon cloth was used as the working electrode. Carbon cloth was subjected to hydrophilic treatment before use, using a tube furnace annealing at 450 °C for 150 min. The samples were prepared by electrodeposition method at a current density of −100 mA cm^{-2} for 200 s. The samples synthesized by adding 0.25, 0.5, 1, and 1.5 mmol $La(NO_3)_3 \cdot 6H_2O$ were named as NiFeLa0.25, NiFeLa, NiFeLa1 and NiFeLa1.5, respectively.

https://doi.org/10.1007/s40820-024-01528-9

2.3 Fabrication of NiFeMo Alloy

The synthesis of NiFeMo follows the same procedure as the above-mentioned synthesis method, with the deposition solution consisting of 0.5 mmol Na_2MoO_4.

2.4 Fabrication of NiFe Alloy

The synthesis of NiFe alloy follows the same procedure as the above-mentioned synthesis method, with the deposition solution consisting of only 15 mmol of $NiCl_2 \cdot 6H_2O$, 5 mmol of $FeCl_3 \cdot 6H_2O$ and 10 mmol of NaCl.

Details on material characterizations, electrochemical measurements and computation methods are provided in supporting information.

3 Results and Discussion

3.1 Characterizations of the Prepared Electrocatalysts

We first develop a straightforward one-step method using in situ electrodeposition technique to synthesize the ternary NiFeM (M: 4*d*-Mo/5*d*-La) catalysts. Based on the inductively coupled plasma optical emission spectroscopy (ICP-OES) results present in Fig. S1, the doping levels of Mo and La in NiFeMo and NiFeLa are consistent, ruling out the influence of different levels of Mo and La on the results. As evidenced by X-ray diffraction (XRD), the diffraction peaks at 44.4°, 51.6°, and 76.2° can be assigned to the (111), (200), and (220) planes of NiFe alloy, respectively (PDF#38–0419) (Fig. 1a). The introduction of La and Mo atoms results in typical varying degrees of variations in XRD peak intensity and peak broadening of the NiFe sample, suggesting the construction of asymmetric M-NiFe units. Additionally, scanning electron microscopy (SEM) images reveal that the NiFe-based samples (NiFe, NiFeMo, and NiFeLa) are all uniformly grown on the carbon cloth (CC) with nanoparticle morphologies (Figs. S2–S4). HAADF-STEM image and energy-dispersive X-ray (EDS) for NiFeLa with elemental mapping images demonstrate the uniform distribution of Ni, Fe, and La elements (Figs. 1b and S5). High-Resolution Transmission Electron Microscope (HRTEM) image and the fast Fourier transform (FFT) pattern indicate the good crystallinity of NiFe alloy (Fig. S6). The TEM images in Figs. 1c and S7 demonstrate the NiFeMo exhibits a polycrystalline structure with part of amorphous areas. The spacing of 2.08 Å is recognized as the (111) plane of NiFeMo. Based on the HRTEM images of NiFeLa in Fig. 2d, it is evident that there exist numerous grain boundaries among the NiFeLa particles, as well as localized ordered regions (marked by the blue dashed lines) with a diameter smaller than 5 nm. In contrast, NiFeMo exhibits compact nanocrystals as well as localized regions with order exceeding 10 nm, align with the XRD results. In addition, the (111) plane of NiFeLa has a larger spacing (2.10 Å), indicating that the introduction of La element leads to more significant lattice distortion (Figs. 2e and S8) [33]. The fine structure of NiFeLa is studied using the HAADF-STEM with aberration correction (AC-HAADF-STEM). In the high-resolution AC-HAADF-STEM image of NiFeLa, the presence of grain boundaries (Fig. 2f, g) and the variation of Ni-M ($M =$ Ni, Fe or La) distance (Fig. 2h, i) further confirm the successful incorporation of La and the distorted structure of NiFeLa [34]. And La atoms are located in the same column as the Ni/Fe atoms, indicating that La replaces the Ni/Fe in the lattice of NiFe. Therefore, it can be considered that this one-step method can effectively induce the dispersion of La atoms within NiFe, disrupting the symmetry of Ni–Fe units and assisting the construction of gradient 3*d*-5*d* orbital coupled Ni/Fe-M asymmetric geometric structure.

X-ray absorption spectroscopy (XAS) is utilized to investigate modifications in both the structural and electronic properties. The X-ray absorption near-edge structure spectra (XANES) at Ni K-edge shown in Fig. 2a, b demonstrate that the absorption threshold position of Ni atom in NiFeLa is higher than that of Ni foil reference and NiFe alloy, suggesting the valence state of Ni increases after the introduction of La [35]. In addition, the Ni K-edge Fourier transforms extended X-ray absorption fine structure (FT-EXAFS) spectra of NiFeLa show three peaks located at about 2.48, 4.05, and 4.7 Å, which can be assigned to the Ni-M bonds (Figs. 2c and S9) [17, 36]. Compared to NiFe, the NiFeLa displays a significant decrease in the peaks' intensity at Ni-M distance, further suggesting the lattice distortion and asymmetric La-Ni/Fe units [37]. The wavelet transform (WT) analysis further offers information in both R- and K-space information of those samples, revealing the overlapping contributions in the radial distance. Additionally, the local

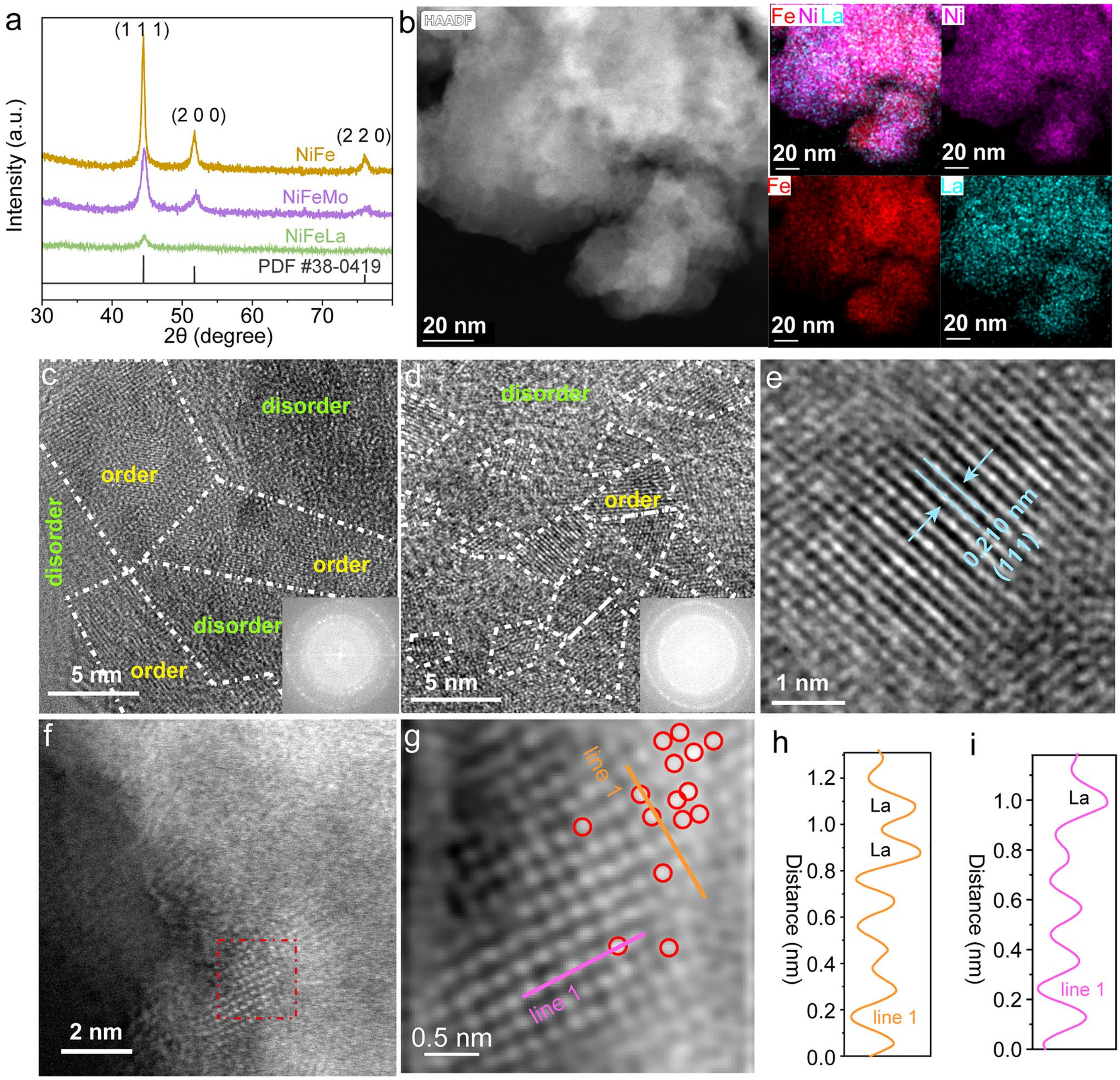

Fig. 1 **a** The XRD patterns of NiFe, NiFeMo and NiFeLa. **b** HAADF-STEM image with elemental mappings of NiFeLa. **c** HRTEM image of NiFeMo. **d, e** HRTEM image of NiFeLa. The insets in (**c, d**) show the FFT patterns of the selected areas. **f, g** AC-HAADF-STEM image of NiFeLa. **h, i** Integrated pixel intensities of the NiFeLa taken from the orange and rose lines in **g**, respectively

coordination environment of Ni is explored using extended X-ray absorption fine structure spectra (EXAFS) along with their respective wavelet-transformed (WT) contour plots (Fig. 2d–f). The relatively longer Ni-M bond located at ~ 7.8 $Å^{-1}$ can be observed in the pattern of NiFeLa, further proving the lattice distortion of NiFeLa [38, 39]. The results from XANES of Fe K-edge for NiFeLa and NiFe shown in Fig. 2g, h, demonstrate the increased valence state of Fe after the introduction of La. Compared with the FT-EXAFS spectra of NiFe, the peak intensity at Fe-M bonds in NiFeLa is notably reduced, indicating the presence of lattice distortion and asymmetric La-Ni/Fe units, which aligns with the FT-EXAFS spectra of the Ni K-edge (Figs. 2i and S10). The relatively longer Fe-M bond observed in the WT contour

https://doi.org/10.1007/s40820-024-01528-9

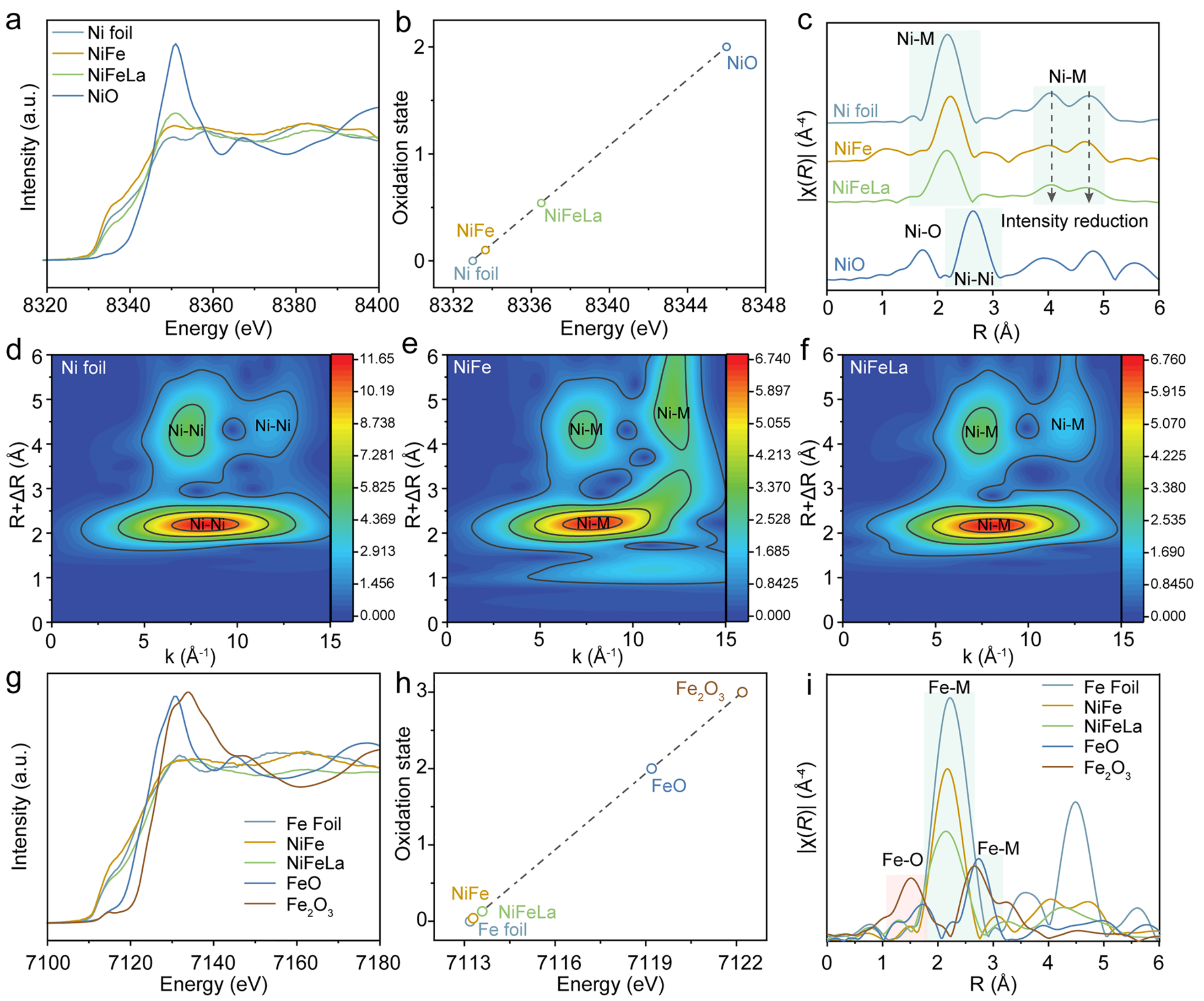

Fig. 2 **a** XANES spectra at the Ni K-edge of NiFe, NiFeLa, Ni foil and NiO. **b** Oxidation state of various Ni species obtained from Ni K-edge XANES. **c** FT-EXAFS of NiFe, NiFeLa, Ni foil and NiO. **d-f** Wavelet transform of Ni K-edge EXAFS data of Ni foil, NiFe and NiFeLa. **g** Ni 2*p* XPS spectra of NiFe and NiFeLa. **h** Fe 2*p* XPS spectra of NiFe and NiFeLa. **i** La 3*d* XPS spectra of NiFeLa

plots of NiFeLa further proving the asymmetric La-Ni/Fe units (Fig. S11). In addition, the fitting curves indicate that as the introduction of La element, the Ni-M ($M=$Ni, Fe, La) and Fe-M bonds move to the structures with low coordination numbers (Tables S1 and S2). The surface chemical states of the NiFe alloy and NiFeLa alloy are further investigated by X-ray photoelectron spectroscopy (XPS) (Fig. S12). Notably, the positive shifts of Ni 2*p* and Fe 2*p* of NiFeLa compared to those of NiFe can be observed, agreeing well with the XAS results [36].

3.2 Electrocatalytic OER Performances

First, the electrocatalytic performance of NiFeLa catalysts with different La ratios is assessed using a conventional three-electrode setup in 1 M KOH electrolyte solution. The content of La in NiFeLaX ($X=0.25$, 0.5, 1, 1.5) determined by ICP-OES are shown in Fig. S13 and Table S3. As depicted in Fig. S14a, the LSV curves reveal that the NiFeLa1.5 exhibits remarkable OER activity, with an overpotential of 185 mV to achieve the current density of 10 mA cm^{-2}, which is much lower than those of NiFe (244 mV), NiFeLa0.25 (201 mV). While there is no significant difference in the overpotential of NiFeLa0.5 (190 mV) and NiFeLa1 (187 mV) compared to that of NiFeLa1.5. Furthermore, as shown in Fig. S14b, NiFeLa0.5, NiFeLa1, and NiFeLa1.5 exhibit the same Tafel slope of 34.3 mV dec^{-1}. Additionally, the long-term stability of the synthesized NiFeLaX ($X = 0.25$, 0.5, 1.5) is further examined within 1 M KOH (Fig. S14c). The chronopotentiometric tests indicate that NiFeLa0.5 exhibits the most outstanding OER stability, maintaining the current density of 1A cm^{-2} for > 100 h, which is longer than those of NiFe, NiFeLa0.25, NiFeLa1 and NiFeLa1.5. As depicted in Fig. S14d, the NiFeLa0.5 possesses the most suitable OER activity and stability. Therefore, we choose NiFeLa0.5 for further comparison and NiFeLa refers to NiFeLa0.5 in the whole text.

The electrocatalytic performances of NiFeLa, NiFeMo and commercial RuO_2 are further evaluated in 1 M KOH electrolyte by using a standard three-electrode system. Figure 3a, b shows that NiFeLa displays the best OER activity, with the overpotential of 190 and 248 mV to achieve the current density of 10 and 100 mA cm^{-2}, respectively, which are significantly lower than those of NiFe (249 and 303 mV), NiFeMo (240 and 294 mV) and commercial RuO_2 (334 and 443 mV). It is noteworthy that the catalytic activity of NiFeLa surpasses most of the reported transition metal-based alkaline electrocatalysts (Fig. 3c and Table S4). The excellent OER activity of NiFeLa is further evidenced by the lowest Tafel slope, suggesting its faster kinetics during the OER process (Fig. 3d) [40]. Furthermore, the electrocatalytic kinetics during the OER process are probed using in situ electrochemical impedance spectroscopy (EIS) measurements, conducted under different applied voltages. As shown in Fig. S15, NiFeLa displays the most diminutive Nyquist semicircle diameter, suggesting the most minimal R_{ct} experienced throughout the OER process. In the Bode phase plots, the highest phase angle peaks observed in the high-frequency and low-frequency regions correspond to the inherent electron conduction of the electrocatalyst and the charge transfer occurring at the interface between the electrolyte and the catalyst, respectively [41]. As shown in Figs. S16–S18, the samples display higher phase peaks at low-frequency regions (~ 0.01–10 Hz) compared to high-frequency regions (~ 100–10,000 Hz), unveiling that the charge transfer is predominantly constrained by the resistance at the electrolyte-catalyst interface. Upon raising the applied potentials from 1.30 to 1.55 V (vs. RHE), the phase angles at low-frequency for NiFeLa demonstrate an accelerated decline trend compared with other catalysts, suggesting La doping facilitates the electron transfer at electrolyte-catalyst interface, leading to superior OER kinetics (Fig. 3e) [42]. In addition, the electrochemically active surface area (ECSA) was conducted to evaluate the electrochemical features of those electrocatalysts by employing double-layer capacitance (C_{dl}) via CV (Fig. S19). As shown in Fig. S19d, NiFeLa displays the highest C_{dl} of 13.4 mF cm^{-2}, indicating the most active site exposure. Additionally, as shown in Table S5, the specific activity, represented by the current density normalized by the electrochemical surface area, further suggests the remarkable catalytic activity of NiFeLa. In addition, to understand the interaction between La and Ni/Fe, in situ ultraviolet (UV) spectra at different potentials are carried out (Fig. S20). The spectra are collected from open circuits potential (OCP) to 1.6 V with an interval of 0.05 V. As shown in Fig. S20a, the spectra of NiFe display a peak appearing at around 350 nm when the potential at 1.4 V and above, which can be attributed to the signal of *OOH-NiFe. The peak located at ~ 450 nm appears from 1.45 V and remains unchanged when the voltage exceeds 1.60 V, identifying the generation of *OO-NiFe [1, 43]. Simultaneously, the spectra of NiFeMo in Fig. S20b demonstrate distinctive peaks at ~ 350 nm when the potential at 1.4 V and above, which can be attributed to the signal of *OOH-NiFeMo. And a broad peak range 400 to 700 nm emerges and remains constant in the OER relevant potential region (≥ 1.45 V), corresponding to *OO-NiFeMo. While prominent peaks can be observed at ~ 350 nm (*OOH-NiFeLa) with a voltage of 1.35 V for NiFeLa (Fig. S20c). It is worth noting that unique peak around ~ 600 nm is observable in the OER-relevant potential range (≥ 1.40 V), corresponding to the accumulation of *OO-NiFeLa. Based on the above results, it can be inferred that NiFeLa is more prone to losing electrons to form *OOH and *OO species at the lowest potential, thereby exhibiting higher OER activity. The electrocatalytic stabilities of NiFeLa and NiFe during OER are also investigated. As shown in Fig. 3f, NiFeLa exhibits an unabated activity similar to its initial state after 2000 cycles of CV. The chronopotentiometric test indicates that the current density of 100 mA cm^{-2} shows negligible degradation for > 600 h, while the stability of the NiFe catalyst decreases significantly (Fig. 3g). Besides, the XRD and XPS spectra of NiFeLa after OER test shown in Figs. S21 and S22 indicate that the NiFeLa catalyst can effectively maintain the structural stability throughout the OER process.

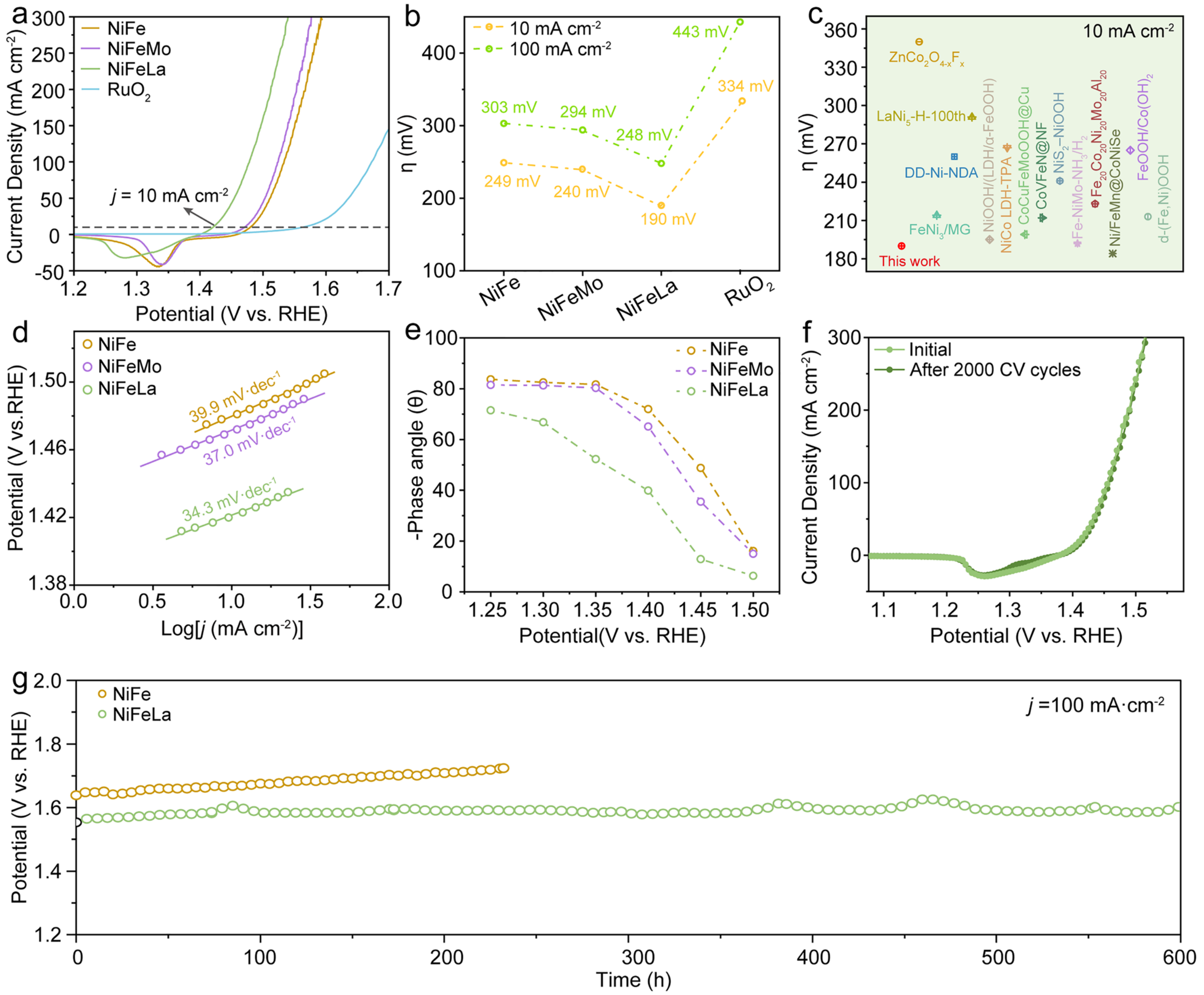

Fig. 3 **a** LSV curves of NiFe, NiFeMo, NiFeLa and commercial RuO_2 in 1 M KOH solution at oxygen-saturated atmosphere. **b** Comparison of the overpotential at the current density of 10 and 100 mA cm^{-2} according to LSV curves. **c** Comparison of the overpotential at the current density of 10 mA cm^{-2} of NiFeLa with recently reported transition metal-based OER electrocatalysts in alkaline electrolyte. **d** Corresponding Tafel plots according to the LSV curves in Fig. 3a. **e** Summarized phase peak angles of NiFe, NiFeMo, and NiFeLa at 1.25–1.50 V. **f** LSV curves of NiFeLa before and after 2000 cycles CV. **g** Chronopotentiometric curves of NiFe and NiFeLa at current density of 100 mA cm^{-2}

3.3 Mechanism Exploration

To in-depth explore the origin of the enhanced OER activity by NiFeLa, the density functional theory with Coulomb interactions (DFT + U) calculations were probed (Figs. S23–S26). We firstly analyzed the adsorption energy of oxygen intermediates on different adsorption sites. The results indicate that it is energetically favorable for the doped La/Mo atoms to replace Ni atoms in NiFe and the oxygen intermediates absorbed on hollow sites, as shown in Figs. S24–S26. Furthermore, it is well known that optimizing the adsorption/desorption of oxygen intermediates is crucial for improving the OER performance of NiFe catalysts in alkaline electrolytes. Thus, the electronic interaction could be considered as the coupling between the adsorbate states and the transition-metal *d* states, which gives rise to the formation of separated bonding and antibonding states. The bonding states are generally fully filled because they are far below the Fermi level (E_f), while the electron filling of the antibonding states depends on these energy states

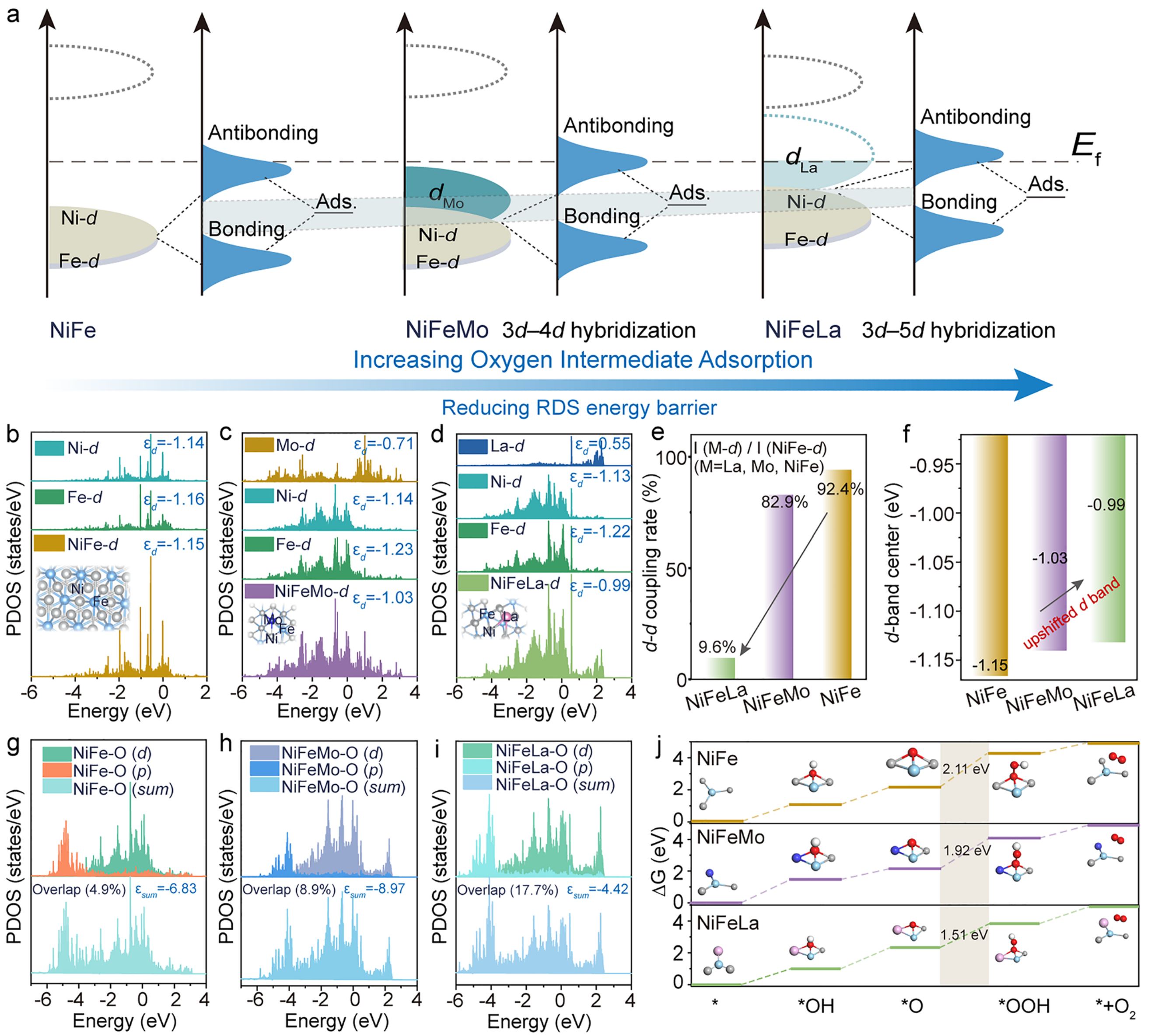

Fig. 4 **a** Schematic illustration of bond formation between the reaction surface and the adsorbate (Ads.). The partial density of states (PDOS) analysis of **b** NiFe, **c** NiFeMo and **d** NiFeLa. **e** *d-d* coupling rate of M (Ni, Mo, La) and Ni/Fe in NiFeLa, NiFeMo, and NiFe. **f** *d*-band center of adsorbed atoms in the NiFe, NiFeMo and NiFeLa. The PDOS analysis of **g** NiFe-O, **h** NiFeMo-O and **i** NiFeLa-O. **j** Free energy diagram of OER on NiFe, NiFeMo, NiFeLa

relative to the Fermi level (i.e., *d* band center) and contributes to the bond strength (Fig. 4a) [44–46]. The *d*-orbital density of states (DOS) of different sites in NiFe/NiFeMo/NiFeLa is further investigated to probe the adsorption strength between the oxygen intermediates and NiFe before and after Mo/La doping (Fig. 4b–d). Specially, benifiting from the mismatch of orbital energy in NiFeLa than those of NiFe and NiFeMo (Fig. 4e), the *d*-band center of adsorbed atoms in the NiFeLa (−0.99 eV) is higher than those in NiFe (−1.15 eV) and NiFeMo (-1.03 eV) (Fig. 4f). Therefore, compared to NiFe and NiFeMo, the antibonding electron of NiFeLa decreases with elevation of antibonding orbitals, resulting in enhanced adsorption strength between oxygen intermediates and NiFeLa. Moreover, as shown in Fig. S27, the La and Mo atoms would lose electrons (negative value), while the NiFe atoms would obtain electrons

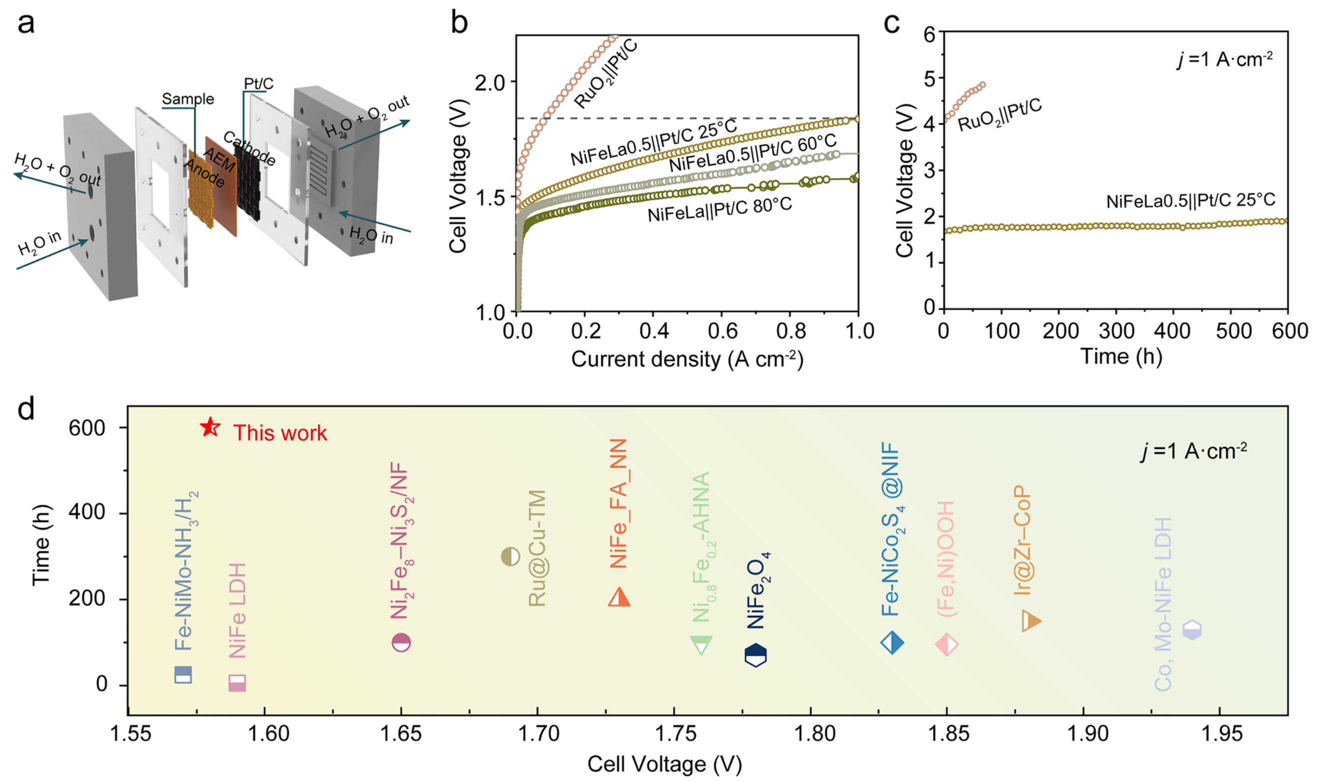

Fig. 5 **a** Schematic illustration of the designed AEM water electrolyzer. **b** LSV curves of AEM water electrolyzer for NiFeLa//Pt/C at 25, 60, and 80 °C, respectively, and commerical RuO_2||Pt/C cells at 25 °C. **c** Durability cell voltage–time plots for the AEM water electrolyzer at a constant current density of 1 A cm^{-2} for 600 h. **d** Comparison the current density of AEM water electrolyzer for the NiFeLa||Pt/C cell and the reported AEM water electrolyzer cells at the current density of 1 A cm^{-2} in 1 M KOH

(positive value). Notably, the charge loss in NiFeLa is much higher than those in NiFe and NiFeMo, further indicating the facilitating the adsorption of adsorbates [47]. Consequently, the adsorption behavior of *OOH-NiFeM in different NiFeM is further calculated. And the enhanced adsorption strength of *OOH in NiFeLa is observed than NiFeMo/NiFe, as indicated by the decreased antibonding electron in NiFeLa-O bond and increased orbital coupling between O-*p* and NiFeLa-*d* (Fig. 4g–i), and the strongest M–O in *OOH-NiFeLa (Fig. S28) [48–50], as well as the largest electron overlaps in *OOH (Fig. S29) and the highest electronic local functions (Fig. S30). As expected, the enhanced adsorption strength of *OOH caused by mismatched 5*d* orbital coupling in NiFeLa is favorable to decrease the rate-determining step (RDS) (*O → *OOH) (Figs. 4j and S31).

To further verify the relationship between different La contents and OER activity and stability, we also conducted DFT calculations with various La doping (Figs. S32-S35). As expected, compared to NiFeLa-1 (with a La content ~ 5%), the *d*-band center of the adsorbed atoms in NiFeLa-2 and NiFeLa-3 catalysts rises with the increased La doping (Fig. S36), thereby gradually enhancing the adsorption of oxygen intermediates (Fig. S37a). Specifically, the energy barriers of PDS remained relatively unchanged with different La doping. However, as the amount of La increases, the surface energy gradually increased (Fig. S37b), indicating a decreased stability with increased La doping, which is consistent with the electrochemical results.

3.4 Electrochemical Evaluation of AEMWE Device

Encouraged by the overall high activity and stability of NiFeLa towards OER, we assemble a single cell using the prepared catalyst as the anode to evaluate its performance in a real AEMWE device (Figs. 5a and S38a). Excitingly, cell voltages of only 1.7/1.83, 1.58/1.68, and 1.52/1.58 V are needed for NiFeLa to reach the current densities of 0.5 and 1 A cm^{-2} at 25, 60, and 80 °C, respectively, much superior to that obtained with commercial RuO_2 (2.05 V@0.2 A cm^{-2}) and NiFe (1.82/2.08, 1.72/1.93, and 1.68/1.84 V) (Figs. 5b and S39). The steady-state polarization curves operated at 25, 60, and 80 °C, demonstrate that the performance of AEMWE can be greatly improved with the utilization of NiFeLa. In addition, the Faraday efficiencies of O_2 production are also measured, which fit well with the theoretical yields with the molar ratio of O_2, indicating a Faraday efficiency of almost 99% (Fig. S38b–d). Furthermore, as shown in Fig. 5c, the NiFeLa cell demonstrates well-maintained AEMWE performance after running for over 600 h under 1 A cm^{-2} with no significant decrease, surpassing commercial RuO_2 and most of the reported transition metal-based catalysts, describing the remarkable OER performance of NiFeLa under practical operation conditions (Fig. 5d and Table S6).

4 Conclusions

In summary, we present a practical concept by constructing asymmetric M-NiFe units to regulate the *d*-orbital and electronic structures of NiFe-based catalysts. The 5*d*-introduced NiFeLa shows remarkable activity and stablility toward OER, as well as long-term operation in AEMWE devices. Experimental results and DFT calculations indicate that the introduction of La atoms into NiFe could disrupt the symmetry of the Ni–Fe units, optimize the *d-p* orbital hybridization between the metal sites on the surface of the catalyst and oxygen-containing intermediates, thereby reducing the RDS energy barrier and boosting the OER performance. This work offers a feasible solution for the practical application of NiFe-based catalysts in commercial AEMWE systems through the electronic regulation strategy induced by *d*-orbital hybridization.

Acknowledgements This work was financially supported by the National Natural Science Foundation of China (22309137, 22279095), and Open subject project State Key Laboratory of New Textile Materials and Advanced Processing Technologies (FZ2023001). We acknowledge the great help from Prof. Weilin Xu and co-workers at Wuhan Textile University for helpful measurements and discussion. We thank the Analytical and Testing Center of Wuhan Textile University for XRD and ICP test.

Author Contribution Xing Wang: Conceptualization, original draft writing, visualization. Wei Pi: Investigation, data curation. Sheng Hu: Validation. Haifeng Bao: Funding acquisition. Na Yao: Investigation, original draft writing, Funding acquisition. Wei Luo: Review, supervision, Funding acquisition.

Declarations

Conflict of interest The authors declare no interest conflict. They have no known competing financial interests or personal relationships that could have appeared to influence the work reported in this paper.

Supplementary Information The online version contains supplementary material available at https://doi.org/10.1007/s40820-024-01528-9.

References

1. R.R. Rao, S. Corby, A. Bucci, M. García-Tecedor, C.A. Mesa et al., Spectroelectrochemical analysis of the water oxidation mechanism on doped nickel oxides. J. Am. Chem. Soc. **144**, 7622–7633 (2022). https://doi.org/10.1021/jacs.1c08152
2. S.Z. Oener, A. Bergmann, B.R. Cuenya, Designing active oxides for a durable oxygen evolution reaction. Nat. Synth. **2**, 817–827 (2023). https://doi.org/10.1038/s44160-023-00376-6
3. K. Yu, H. Yang, H. Zhang, H. Huang, Z. Wang et al., Immobilization of oxyanions on the reconstructed heterostructure evolved from a bimetallic oxysulfide for the promotion of oxygen evolution reaction. Nano-Micro Lett. **15**, 186 (2023). https://doi.org/10.1007/s40820-023-01164-9
4. F. Zeng, C. Mebrahtu, L. Liao, A.K. Beine, R. Palkovits, Stability and deactivation of OER electrocatalysts: a review. J. Energy Chem. **31**, 301–329 (2022). https://doi.org/10.1016/j.jechem.2022.01.025
5. L. Chong, G. Gao, J. Wen, H. Li, H. Xu et al., La- and Mn-doped cobalt spinel oxygen evolution catalyst for proton exchange membrane electrolysis. Science **380**, 609–616 (2023). https://doi.org/10.1126/science.ade1499

6. P. Wang, T. Yu, L. Hao, X. Liu, P vacancies at the crystalline-amorphous interface of NiFe(OH)$_x$/NiP$_x$/NF enhance the catalytic activity of the oxygen evolution reaction. J. Power. Sources **589**, 233749 (2024). https://doi.org/10.1016/j.jpowsour.2023.233749
7. X. Wang, S. Xi, P. Huang, Y. Du, H. Zhong et al., Pivotal role of reversible NiO$_6$ geometric conversion in oxygen evolution. Nature **611**, 702–708 (2022). https://doi.org/10.1038/s41586-022-05296-7
8. J. Li, Oxygen evolution reaction in energy conversion and storage: design strategies under and beyond the energy scaling relationship. Nano-Micro Lett. **14**, 112 (2022). https://doi.org/10.1007/s40820-022-00857-x
9. H. Lei, L. Ma, Q. Wan, S. Tan, B. Yang et al., Promoting surface reconstruction of NiFe layered double hydroxide for enhanced oxygen evolution. Adv. Energy Mater. **12**, 2202522 (2022). https://doi.org/10.1002/aenm.202202522
10. D. Liu, Y. Yan, H. Li, D. Liu, Y. Yang et al., A template editing strategy to create interlayer-confined active species for efficient and durable oxygen evolution reaction. Adv. Mater. **35**, e2203420 (2023). https://doi.org/10.1002/adma.202203420
11. X. Ren, Y. Zhai, P. Wang, Z. Xu, S. Gao et al., Surface restructuring of zeolite-encapsulated halide perovskite to activate lattice oxygen oxidation for water electrolysis. Adv. Mater. **35**, e2301166 (2023). https://doi.org/10.1002/adma.202301166
12. P. Zhai, C. Wang, Y. Zhao, Y. Zhang, J. Gao et al., Regulating electronic states of nitride/hydroxide to accelerate kinetics for oxygen evolution at large current density. Nat. Commun. **14**, 1873 (2023). https://doi.org/10.1038/s41467-023-37091-x
13. L. Magnier, G. Cossard, V. Martin, C. Pascal, V. Roche et al., Fe–Ni-based alloys as highly active and low-cost oxygen evolution reaction catalyst in alkaline media. Nat. Mater. **23**, 252–261 (2024). https://doi.org/10.1038/s41563-023-01744-5
14. M. Zhao, W. Li, J. Li, W. Hu, C.M. Li, Strong electronic interaction enhanced electrocatalysis of metal sulfide clusters embedded metal-organic framework ultrathin nanosheets toward highly efficient overall water splitting. Adv. Sci. **7**, 2001965 (2020). https://doi.org/10.1002/advs.202001965
15. Y. Zhao, W. Wan, N. Dongfang, C.A. Triana, L. Douls et al., Optimized NiFe-based coordination polymer catalysts: sulfur-tuning and operando monitoring of water oxidation. ACS Nano **16**, 15318–15327 (2022). https://doi.org/10.1021/acsnano.2c06890
16. C. Li, E. Lepre, M. Bi, M. Antonietti, J. Zhu et al., Oxygen-rich carbon nitrides from an eutectic template strategy stabilize Ni, Fe nanosites for electrocatalytic oxygen evolution. Adv. Sci. **10**, e2300526 (2023). https://doi.org/10.1002/advs.202300526
17. H. Meng, B. Wu, T. Sun, L. Wei, Y. Zhang et al., Oxidization-induced structural optimization of Ni$_3$Fe–N–C derived from 3D covalent organic framework for high-efficiency and durable oxygen evolution reaction. Nano Res. **16**, 6710–6720 (2023). https://doi.org/10.1007/s12274-023-5475-7
18. Q. Zhou, C. Xu, J. Hou, W. Ma, T. Jian et al., Duplex interpenetrating-phase FeNiZn and FeNi$_3$ heterostructure with low-Gibbs free energy interface coupling for highly efficient overall water splitting. Nano-Micro Lett. **15**, 95 (2023). https://doi.org/10.1007/s40820-023-01066-w
19. M.K. Adak, L. Mallick, K. Samanta, B. Chakraborty, Slow O-H dissociation in the first-order oxygen evolution reaction kinetics on polycrystalline γ-FeO(OH). J. Phys. Chem. C **127**, 154–168 (2023). https://doi.org/10.1021/acs.jpcc.2c08107
20. J. Hu, Q. Xu, X. Wang, X. Huang, C. Zhou et al., Charge-transfer-regulated bimetal ferrocene-based organic frameworks for promoting electrocatalytic oxygen evolution. Carbon Energy **5**, e315 (2023). https://doi.org/10.1002/cey2.315
21. L. Zhao, J. Yan, H. Huang, X. Du, H. Chen et al., Regulating electronic structure of bimetallic NiFe-THQ conductive metal–organic frameworks to boost catalytic activity for oxygen evolution reaction. Adv. Funct. Mater. **34**, 2310902 (2024). https://doi.org/10.1002/adfm.202310902
22. Y. Zhu, X. Wang, X. Zhu, Z. Wu, D. Zhao et al., Improving the oxygen evolution activity of layered double-hydroxide via erbium-induced electronic engineering. Small **19**, e2206531 (2023). https://doi.org/10.1002/smll.202206531
23. Y. Zhang, W. Zhang, X. Zhang, X. Wang, J. Wang et al., Activating lattice oxygen based on energy band engineering in oxides for industrial water/saline oxidation. Energy Environ. Sci. **17**, 3347–3357 (2024). https://doi.org/10.1039/d4ee00214h
24. X. Zhao, Y. Sun, J. Wang, A. Nie, G. Zou et al., Regulating d-orbital hybridization of subgroup-IVB single atoms for efficient oxygen reduction reaction. Adv. Mater. **36**, e2312117 (2024). https://doi.org/10.1002/adma.202312117
25. B. Guo, Y. Ding, H. Huo, X. Wen, X. Ren et al., Recent advances of transition metal basic salts for electrocatalytic oxygen evolution reaction and overall water electrolysis. Nano-Micro Lett. **15**, 57 (2023). https://doi.org/10.1007/s40820-023-01038-0
26. Z. Zhang, C. Liu, C. Feng, P. Gao, Y. Liu et al., Breaking the local symmetry of LiCoO$_2$ via atomic doping for efficient oxygen evolution. Nano Lett. **19**, 8774–8779 (2019). https://doi.org/10.1021/acs.nanolett.9b03523
27. J.-H. Huang, Y. Si, X.-Y. Dong, Z.-Y. Wang, L.-Y. Liu et al., Symmetry breaking of atomically precise fullerene-like metal nanoclusters. J. Am. Chem. Soc. **143**, 12439–12444 (2021). https://doi.org/10.1021/jacs.1c05568
28. M. Li, X. Wang, K. Liu, H. Sun, D. Sun et al., Reinforcing Co–O covalency via Ce(4f)─O(2p)─Co(3d) gradient orbital coupling for high-efficiency oxygen evolution. Adv. Mater. **35**, e2302462 (2023). https://doi.org/10.1002/adma.202302462
29. Q. Zhang, W. Zhang, J. Zhu, X. Zhou, G.-R. Xu et al., Tuning d–p orbital hybridization of NiMoO$_4$@Mo$_{15}$Se$_{19}$/NiSe$_2$ core-shell nanomaterials via asymmetric coordination interaction enables the water oxidation process. Adv. Energy Mater. **14**, 2304546 (2024). https://doi.org/10.1002/aenm.202304546
30. X. Zhong, L. Sui, M. Yang, T. Koketsu, M. Klingenhof et al., Stabilization of layered lithium-rich manganese oxide for anion exchange membrane fuel cells and water electrolysers. Nat. Catal. **7**, 546–559 (2024). https://doi.org/10.1038/s41929-024-01136-1

31. B. Zhang, L. Wang, Z. Cao, S.M. Kozlov, F.P. García de Arquer et al., High-valence metals improve oxygen evolution reaction performance by modulating 3d metal oxidation cycle energetics. Nat. Catal. **3**, 985–992 (2020). https://doi.org/10.1038/s41929-020-00525-6
32. S. Zhao, F. Hu, L. Yin, L. Li, S. Peng, Manipulating electron redistribution induced by asymmetric coordination for electrocatalytic water oxidation at a high current density. Sci. Bull. **68**, 1389–1398 (2023). https://doi.org/10.1016/j.scib.2023.06.001
33. S. Liu, W. Qi, J. Liu, X. Meng, S. Adimi et al., Modulating electronic structure to improve the solar to hydrogen efficiency of cobalt nitride with lattice doping. ACS Catal. **13**, 2214–2222 (2023). https://doi.org/10.1021/acscatal.2c05075
34. W. Tian, J. Han, L. Wan, N. Li, D. Chen et al., Enhanced piezocatalytic activity in ion-doped SnS_2 via lattice distortion engineering for BPA degradation and hydrogen production. Nano Energy **107**, 108165 (2023). https://doi.org/10.1016/j.nanoen.2023.108165
35. Y.-N. Zhou, F.-T. Li, B. Dong, Y.-M. Chai, Double self-reinforced coordination modulation constructing stable Ni^{4+} for water oxidation. Energy Environ. Sci. **17**, 1468–1481 (2024). https://doi.org/10.1039/d3ee02627b
36. L. Wu, M. Ning, X. Xing, Y. Wang, F. Zhang et al., Boosting oxygen evolution reaction of (Fe, Ni)OOH via defect engineering for anion exchange membrane water electrolysis under industrial conditions. Adv. Mater. **35**, e2306097 (2023). https://doi.org/10.1002/adma.202306097
37. M. Cai, Q. Zhu, X. Wang, Z. Shao, L. Yao et al., Formation and stabilization of NiOOH by introducing α-FeOOH in LDH: composite electrocatalyst for oxygen evolution and urea oxidation reactions. Adv. Mater. **35**, e2209338 (2023). https://doi.org/10.1002/adma.202209338
38. J. Zhang, D. Wong, Q. Zhang, N. Zhang, C. Schulz et al., Reducing Co/O band overlap through spin state modulation for stabilized high capability of 4.6 V $LiCoO_2$. J. Am. Chem. Soc. **145**, 10208–10219 (2023). https://doi.org/10.1021/jacs.3c01128
39. H. Li, P. Shi, L. Wang, T. Yan, T. Guo et al., Cooperative catalysis of polysulfides in lithium-sulfur batteries through adsorption competition by tuning cationic geometric configuration of dual-active sites in spinel oxides. Angew. Chem. Int. Ed. **62**, 2216286 (2023). https://doi.org/10.1002/anie.202216286
40. L. Deng, S.-F. Hung, Z.-Y. Lin, Y. Zhang, C. Zhang et al., Valence oscillation of Ru active sites for efficient and robust acidic water oxidation. Adv. Mater. **35**, e2305939 (2023). https://doi.org/10.1002/adma.202305939
41. S. Zhou, H. He, J. Li, Z. Ye, Z. Liu et al., Regulating the band structure of Ni active sites in few-layered NiFe-LDH by *in situ* adsorbed borate for ampere-level oxygen evolution. Adv. Funct. Mater. **34**, 2313770 (2024). https://doi.org/10.1002/adfm.202313770
42. S. Zuo, Z.-P. Wu, H. Zhang, X.W. Lou, Operando monitoring and deciphering the structural evolution in oxygen evolution electrocatalysis. Adv. Energy Mater. **12**, 2103383 (2022). https://doi.org/10.1002/aenm.202103383
43. S. Lee, Y.-C. Chu, L. Bai, H.M. Chen, X. Hu, Operando identification of a side-on nickel superoxide intermediate and the mechanism of oxygen evolution on nickel oxyhydroxide. Chem Catal. **3**, 100475 (2023). https://doi.org/10.1016/j.checat.2022.11.014
44. Z. Chen, Y. Song, J. Cai, X. Zheng, D. Han et al., Tailoring the d-band centers enables Co_4N nanosheets to be highly active for hydrogen evolution catalysis. Angew. Chem. Int. Ed. **57**, 5076–5080 (2018). https://doi.org/10.1002/anie.201801834
45. Y. Zhou, Q. Gu, K. Yin, Y. Li, L. Tao et al., Engineering eg orbital occupancy of Pt with Au alloying enables reversible $Li-O_2$ batteries. Angew. Chem. Int. Ed. **61**, e202201416 (2022). https://doi.org/10.1002/anie.202201416
46. J.K. Nørskov, F. Studt, F. Abild-Pedersen, T. Bligaard, *Fundamental concepts in heterogeneous catalysis* (John Wiley & Sons, NJ, 2014)
47. L. Zhuang, Y. Jia, H. Liu, X. Wang, R.K. Hocking et al., Defect-induced Pt-Co-Se coordinated sites with highly asymmetrical electronic distribution for boosting oxygen-involving electrocatalysis. Adv. Mater. **31**, e1805581 (2019). https://doi.org/10.1002/adma.201805581
48. H. Wang, T. Zhai, Y. Wu, T. Zhou, B. Zhou et al., High-valence oxides for high performance oxygen evolution electrocatalysis. Adv. Sci. **10**, 2301706 (2023). https://doi.org/10.1002/advs.202301706
49. H. Chen, L. Shi, K. Sun, K. Zhang, Q. Liu et al., Protonated iridate nanosheets with a highly active and stable layered perovskite framework for acidic oxygen evolution. ACS Catal. **12**, 8658–8666 (2022). https://doi.org/10.1021/acscatal.2c01241
50. L. Zhang, H. Jang, H. Liu, M.G. Kim, D. Yang et al., Sodium-decorated amorphous/crystalline RuO_2 with rich oxygen vacancies: a robust pH-universal oxygen evolution electrocatalyst. Angew. Chem. Int. Ed. **60**, 18821–18829 (2021). https://doi.org/10.1002/anie.202106631